Miniaturized, Field-deployable, Continuous Soil Water Potential Sensor

Yuncong Chen, Yang Tian, Xinran Wang, Le Wei, and Liang Dong*

***Abstract*—Soil water potential is a significant factor in determining the dynamics of water in the soil. However, few soil water potential sensors are available to conduct long-term, continuous measurements with full automation, due to cavitation formation inside the sensors while interacting with the soil. This paper presents a miniature, field-deployable soil water potential sensor capable of real-time measurement with a wide dynamic range from 0 to -800 kPa, a minimum detectable change of water potential of ~40 Pa, and a high sensitivity of ~0.248 μA/kPa. The sensor consists of a shallow water reservoir sandwiched between a nanoporous ceramic plate and a thin silicon diaphragm with thermal oxide. The nanoscale pores of the ceramic plate allow for the increase of air entry tension, while the smooth and hydrophilic interior surfaces of the water reservoir help to minimize the trapping of air bubbles in the reservoir. When the sensor is embedded in unsaturated soils, the pre-filled water in the reservoir tends to leave the reservoir through the nanopores of the ceramic plate, until an equilibrium in water potential is achieved between the reservoir and the soil. The loss of water leads to bending of the silicon-based diaphragm toward the reservoir. The displacement of the diaphragm is quantified by a miniature optical displacement detector assembled with the sensor, which corresponds to the soil water potential. The presented soil sensor has been validated through both greenhouse and field experiments to monitor dynamic changes in soil water potential in real-time over multiple days.**

***Index Terms*—Agricultural sensor, in-situ measurement, photodetector, soil water potential.**

I. Introduction

WATER transport in soils is best described as being driven by gradients of water potential. Soil water potential is one of the main factors in determining the dynamics of water in soils. Infrequent or light watering leads to drought conditions and water stress on plants, while over-irrigation causes nutrient leaching, water loss, and anaerobic soil conditions [1]-[3]. For instance, soils with excess water often have a lower oxygen concentration causing stomatal closure of crops and insufficient transpiration even in the presence of water in soils [4]. Precision water management is thus always desirable for agriculture as it directly impacts on crop yield while restricting the water and energy input [5]. Continuous monitoring of soil water potential can help us to make water management more efficient and sustainable and cost-effective by providing data to determine "when" and "how much" irrigation should be applied. Further, real-time water potential data will improve our understanding of the soil-plant-atmosphere system [6].

Existing approaches to monitoring of soil water potential can be classified into indirect and direct means. The indirect method measures the percentage of water content in the soil to estimate soil water potential, and requires determination of a genuine relationship between water content and water potential specific for each soil type [7]. For example, soil psychrometers work based on measuring the rate of temperature changes induced by the evaporation and condensation of a water droplet attached on a temperature sensor [8][9]. They can only measure at large depths to reach thermal equilibrium of the small psychrometer chambers, but they cannot be used in saturated soils. For electrical conductivity-based soil water potential sensors, they work under the principle of measuring changes in electrical properties of soils under different wetness conditions [10]; however, soil samples obtained from different locations, even with the same water content, often do not have the same water potential [11], rendering this method a low-accuracy technique [12]. Therefore, the indirect water potential detection methods can only provide relatively coarse information on the soil water status.

In the category of direct measurement methods for soil water potential, pressure plates and tensiometers are widely used. The pressure plate requires gradually applying an external pressure to a soil sample placed inside a chamber until the excess water starts flowing out of the soil [13][14]; this method, however, is limited to laboratory tests and only provides discrete water retention curves. In contrast, the tensiometer operates on the principle of establishing a pressure equilibrium between a water-filled tube (i.e., water reservoir) and surrounding soils through a porous ceramic cup [15]. The direct contact of the cup with unsaturated soils leads to a loss of water from the water reservoir through the ceramic cup, thus inducing a negative pressure inside the reservoir that equals the water potential of the surrounding soil. Although tensiometers have been used to measure water potential in fields, they usually have a relatively bulky size, require frequent refilling of water to compensate for

Department of Electrical and Computer Engineering, Iowa State University, Ames, Iowa 50011.
*Email: ldong@iastate.edu

water depletion [16], and have a relatively limited dynamic range from the saturation to nearly -100 kPa due to a critical cavitation issue [17][18]. More specifically, when cavitation is formed in the water reservoir of the tensiometer, the device becomes dysfunctional [19]. The reason for cavitation is associated with undissolved air nuclei trapped inside the voids of the interior surface or concave corners of the reservoir [20]. Under a negative pressure built inside the water reservoir, the trapped air nuclei tend to grow into large air bubbles, thus blocking the pores embedded in the ceramic cup of the sensor. By making the interior surface smoother and the reservoir volume smaller, it is possible to minimize cavitation formation [21]. But, significantly reducing the size of the reservoir would adversely make it hard to fill water into the reservoir [22]. Different hydrophilic polymers have been used to replace the water in the reservoir for reducing the impact of the formed negative pressure on the trapped air nuclei; this method, however, suffers from a long waiting time to reach pressure equilibration [23]. Further, increasing the air-entry value (AEV, defined as the maximum holding pressure of a channel, above which air bubbles permeate through the channel) of the porous ceramic cup has been proven effective to minimize the penetration of air bubbles and maximize the dynamic range of water potential [24-26]. Despite these remarkable efforts, it is still challenging to realize continuous, field-deployable water potential sensors with high accuracy and a sufficient dynamic range [27] [28].

This paper reports a miniaturized soil sensor for continuous, in-situ monitoring of water potential in fields. We demonstrate that by seamlessly integrating a high-AEV ceramic plate, a flexible silicon diaphragm, a shallow water reservoir with smooth and hydrophilic interior surfaces, and a sensitive optical displacement detector, it is possible to obtain a continuous soil water potential sensor with wide dynamic range and long lifetime for field applications.

II. Structure, Design and Simulation

Fig. 1 shows the proposed miniature soil water potential sensor. The sensor has a shallow water reservoir (depth: 200 μm) sandwiched between a nanoporous alumina (Al_2O_3)-based ceramic plate (thickness: 2 mm; mean pore size: ~80 nm; Cobra Technologies BV) and a 200 μm-thick double-side polished crystalline silicon (Si) diaphragm with 300 nm-thick thermal oxide (SiO_2) grown on both sides of the diaphragm. Here, nanoporous alumina is a proven, commonly used material for the ceramic cups or filters of tensiometers [19][23][29], while the Si/SiO_2 diaphragm allows for easy manufacturing of the sidewalls of the water reservoir by using SU-8 photoresist (thickness: 200 μm) through photolithography. A printed circuit board (PCB) is mounted with a commercial miniature optical displacement detector (OPR5005, TT Electronics), and then is adhered to the water reservoir with 2 mm-thick spacers by using an electronic assembly liquid adhesive (Scotch-Weld™ Structural Adhesive, 3M). The spacers are 3D printed (printer: Form 2, Formlabs) with methacrylate photopolymer-based resin. Both the reservoir and the nanopores are filled with water. Because the nanopores offer a high air-entry tension, this will increase the pressure required for air bubbles to get into the nanopores.

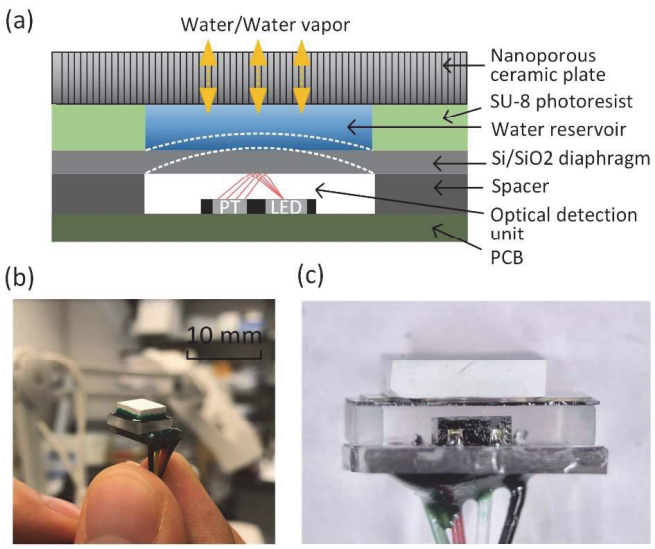

Fig. 1. (a) Cross-sectional schematic representation of the soil water potential sensor. The sensor consists of a nanoporous ceramic plate, a shallow water reservoir, a double-side polished Si/SiO_2 diaphragm, and a PCB with an optical displacement detector. The diaphragm bends when the sensor interacts with unsaturated soils. PT: photodetector; LED: light-emitting device. (b)-(c) Images showing the fabricated soil water potential sensor.

When the sensor is embedded in unsaturated soils, the water potential in the reservoir becomes higher than that of the soil. Therefore, a gradient of water potential is formed across the thickness of the ceramic plate. This gradient drives water transport from inside to outside of the reservoir through the nanopores until an equilibrium in water potential is establihsed between the reservoir and the soil. Consequently, a negative pressure develops in the reservoir, causing the Si/SiO_2 diaphragm to bend towards the reservoir. The displacement of the diaphragm is quantified by the optical displacement detector. In brief, this displacement detector consists of a light-emitting device and a photodetector. The light intensity reflected from the diaphragm is inversely proportional to the square of the distance from the light source to the photodetector [30]. The change in current output from the photodetector correlates to the displacement of the diaphragm, and thus the corresponding change in soil water potential.

To provide a wide dynamic range of soil water potential, the sensor needs to be designed to restrict air invasion into the reservoir. Therefore, the nanopores of the ceramic plate must have an AEV higher than the water potential of interest. Here, the AEV can be expressed as [31]

$$AEV = P_{atmosphere} - P_{water\_reservoir} = \frac{2\sigma cos\theta}{r} > |\psi_{soil}| \quad (1),$$

where $P_{atmosphere}$ is the atmospheric pressure, $P_{water\_reservoir}$ is the pressure in the water reservoir, σ is the surface tension of water (0.072 N/m), θ is the contact angle of water with the inner wall of the nanopore, r is the radius of the nanopore, and ψ_{soil} is the soil water potential. The used ceramic plate has a mean pore radius of 40 nm and a water contact angle of ~60° [32]. Therefore, the AEV of the nanopores is estimated to be ~1.8

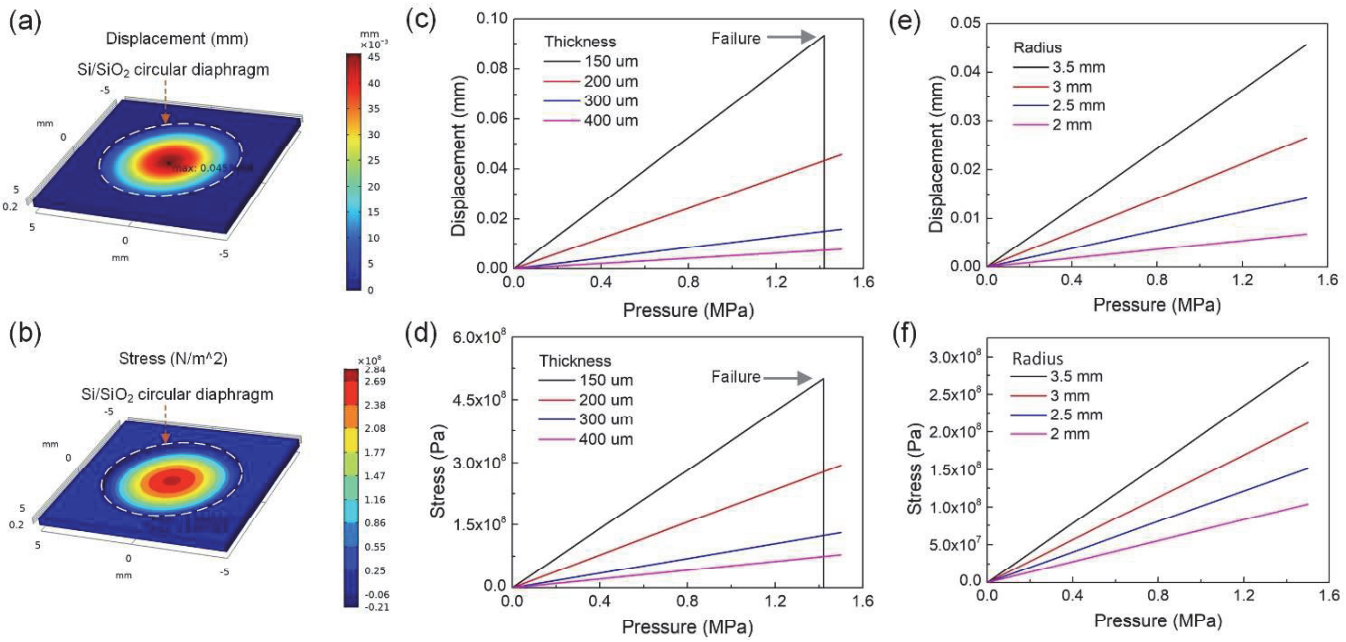

Fig. 2. FEA-based mechanical simulation for the Si/SiO_2 diaphragm of the water reservoir of the sensor. (a) Displacement and (b) stress distribution of a 3.5 mm-radius diaphragm under a 1.5 MPa pressure normally applied to the diaphragm towards the water reservoir. (c) Displacement and (d) stress distribution of the 3.5 mm-radius diaphragm with different thicknesses of 150, 200, 300 and 400 μm, as a function of pressure application. (e) Displacement and (f) stress distribution of the 200 μm-thick diaphragm with different radii of 2, 2.5, 3, and 3.5 mm, as a function of pressure application.

MPa, which is large enough to cover even the wilting point of soil $|\psi_{wilt}|$ = 1.5 MPa for crops [33].

To estimate the influence of varying soil water potential on the displacement of the Si/SiO_2 diaphragm, finite element analysis (FEA)-based simulations were performed using COMSOL Multiphysics software (Fig. 2a and 2b). Different pressures (ranging from 0 to $|\psi_{wilt}|$=1.5 MPa) were normally applied to the diaphragm with different radii (2, 2.5, 3 and 3.5 mm) and thicknesses (150, 200, 300, and 400 μm). Fig. 2c and 2d show the simulated results for both the displacement and stress distribution on a 3.5 mm-radius diaphragm with different thicknesses. Compared to the thicker membranes, the thinner ones can bend more but produce higher mechanical stresses. According to the mechanical characterization in failure strength of crystalline silicon dice [34], thicker silicon dices are more rigid but easier to break when subjected to a bending load; with increasing thickness of silicon dice, the failure stress of the dice increases (until the thickness reaches 200 μm) and then turns to decrease. Because the 150 μm-thick, 3.5 mm-radius silicon diaphragm has a ~500 MPa failure stress [34], the maximum allowed pressure that this diaphragm can withstand is ~1.4 MPa, which is still not large enough to reach $|\psi_{wilt}|$. The 300 μm- and 400 μm-thick diaphragms with the same 3.5 mm radius have lower failure stresses [34] and fewer deflections than the 150 μm-thick counterparts. When a 1.5 MPa pressure (i.e., $|\psi_{wilt}|$) is applied to the 200 μm-thick, 3.5 mm-radius silicon diaphragm, it produces a moderate but sufficient deflection; the maximum stress on this diaphragm is ~293 MPa, which is much less than a ~1000 MPa failure stress of the 200 μm-thick silicon dice [34]. Further, Fig. 2e and 2f show the pressure-induced deflection and stress of the 200 μm-thick diaphragm with different radii. With increasing radius, the diaphragm deflects more, which is beneficial to obtain high sensitivity of the sensor responding to changes in water potential; however, increasing the diaphragm area will also lead to an increase in stress on the diaphragm. To ensure the safe operation of the sensor in field conditions, we chose 3.5 mm as the radius of the diaphragm for the sensor, although there is room to further increase the radius of the 200 μm-thick diaphragm until the maximum stress on the diaphragm at $|\psi_{wilt}|$ reaches the failure stress of ~1000 MPa of the silicon diaphragm.

III. Fabrication, Calibration and Characterization

The fabrication process of the sensor is briefly described in Fig. 3. First, 300 nm-thick thermal oxide layers were grown on both sides of a double-side polished, 200 um-thick Si wafer. Subsequently, a 200 nm-thick SU-8 photoresist layer was spin coated on the surface of the SiO_2 layer and then patterned using photolithography. Thus, a 3.5 mm-radius water reservoir was formed (Fig. 3a-3c). Then, the opening of the water reservoir was covered by a 2 mm-thick nanoporous Al_2O_3 ceramic plate (mean pore size: ~80 nm) with the help of a thin layer of water-proof epoxy (Fig. 3d). To inject water into the reservoir through the ceramic plate, the sensor was placed inside a high-pressure chamber containing deionized water (Fig. 3e). A positive high pressure was applied to the chamber using a piston pump (High Pressure Equipment Co.) at a speed of 1 bar/min until 60-bar pressure was reached. The high pressure retained for 24 h, because complete dissolution of a volume of air into an equal volume of water would occur around 60 bars at room temperature (20 °C). Applying higher pressures would fracture

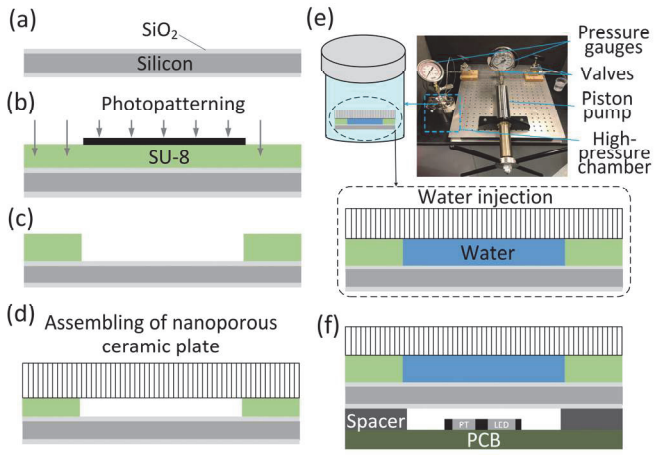

Fig. 3. Manufacturing process flow of the soil water potential sensor. (a) Thermal oxidation of silicon. (b)-(c) Micropatterning of SU-8 photoresist via photolithography. (d) Assembling of nanoporous ceramic plate and SU-8 structures. (e) Injection of water into the water reservoir using the setup displayed in the photo. (f) Assembling of the obtained parts with the PCB-based optical displacement detector to form the final sensor.

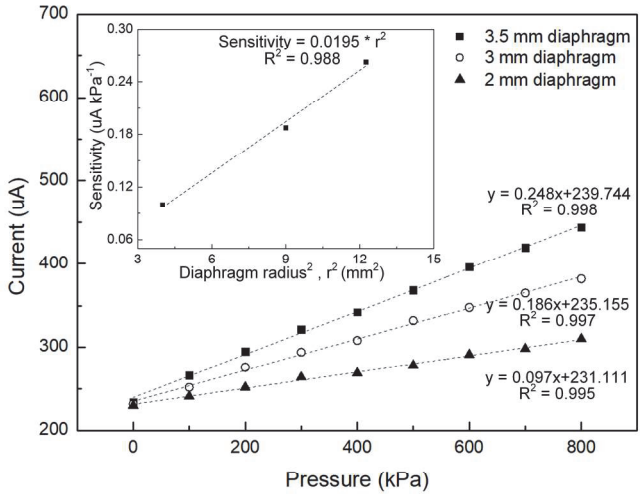

Fig. 4. Calibration of the soil water potential sensors with 2, 3, and 3.5 mm diaphragm radii. The electric current was obtained from the optical displacement detection unit when a positive pressure was applied to the sensor. The inset shows the sensitivity of the sensor as a function of square of the diaphragm radius.

the ceramic plate of the sensor. Finally, a commercial miniature optical displacement detector was surface mounted onto a PCB, and then was attached to the back of the diaphragm through 2 mm-thick spacer (Fig. 3f).

Fig. 4 shows the calibration of the sensor at 20 °C. Here, for the calibration, the sensor, prior to the water injection into the reservoir, was first submerged in deionized water for ~1 h so as to fill the nanopores with DI water and use the water-filled nanopores to seal the air inside the reservoir. It should be noted that when the nanopores were fully filled with water, the Si/SiO_2 diaphragm was seen flat; rinsing the sensor in water for a longer time would not cause an initial displacement of the diaphragm, and thus would not lead to any baseline shift of output signals. After water filling was completed, the device was placed in an air chamber, where different positive air pressures could be applied. The deflections of the Si/SiO_2 diaphragm of the sensor resulting from the applied air pressures could be readout by the optical displacement detector. It should be explicitly noted here that the change of the air pressure difference between outside and inside the reservoir (or the air chamber-to-air-filled reservoir pressure difference) was imitated as that of the water potential difference between the water-filled reservoir and the surrounding soil (or the unsaturated soil-to-water reservoir pressure difference). During the calibration, the air pressure increased up to 800 kPa, and the output current from the photodetector was recorded. The sensitivity of the sensor to the applied pressure was 0.097, 0.187, and 0.248 μA/kPa, for the diaphragm radius of 2, 3, and 3.5 mm, respectively. The sensitivity is nearly linear to the radius squared, thus the area of the diaphragm (see the inset of Fig. 4). We also note that the minimum detectable change of water potential ΔP_{min} is mainly determined by the minimum detectable change of current ΔI_{min} of the data logger of the sensor. Here, because $\Delta I_{min} = 0.01$ μA, ΔP_{min} was calculated to be ~40 Pa for the sensor with the 3.5 mm diaphragm radius, by using the fit of the equation: $y = 0.248x + 239.744$, as displayed in Fig. 4.

Next, the influence of environmental temperature on the output of the fabricated sensor was examined. As the environmental temperature changed from 10 to 35 °C, the output current of the sensor only exhibited a negligibly small reduction by 2.3 ± 1.2%, compared to that obtained at 20 °C. The sensitivity of the sensor to applied pressure (or the slope of the calibration curves in Fig. 4) was found almost insensitive to the temperature change over the above-mentioned range. Therefore, the temperature effect on the sensor could be almost neglected in the field measurement. Such minor temperature effect might be attributed to adopting the structurally symmetrical Si/SiO_2 diaphragm design that is beneficial to reduce undesired temperature fluctuation-induced bending of the diaphragm. In addition, because the total volume of the used reservoir is small, the net volume change due to temperature turns out to be minor.

Fig. 5a demonstrates the dynamic water potential range of the sensor with the 3.5 mm diaphragm radius, based on a free evaporation test, where the sensor was exposed to air and no soils were on the surface of the ceramic plate. As the water in the reservoir gradually evaporated through the nanopores of the ceramic plate, the water potential inside the reservoir became negative, and the Si/SiO_2 diaphragm gradually bent to establish a pressure equilibrium between the inside and outside of the water reservoir. As the potential inside the reservoir went further down to a point around -800 kPa, the undissolved air nuclei in water became inflated enough to come out from the reservoir through the nanopores of the ceramic plate. As a result, the diaphragm was found to deflect back to its original flat state at approximately 240 sec.

Fig. 5b illustrates the experimental setup for conducting a cyclic water potential test on a soil specimen. The setup has a home-made pressure chamber, in which a 2 mm-thick, 5 cm-

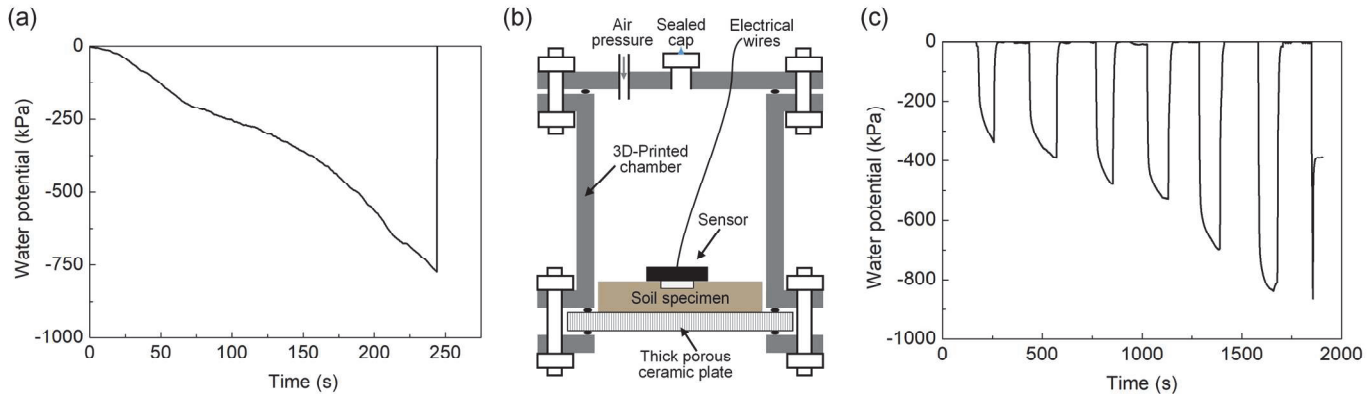

Fig. 5. (a) Free evaporation test result showing the transient response of the sensor when exposed directly to air. (b) Schematic of cyclic evaporation measurement setup. (c) Measured water potential of the soil specimen by applying multiple cycles of positive air pressures. The experiment setup is shown in (b).

diameter ceramic disc (material: Al_2O_3; AEV: 18 bars) was assembled at the bottom as a porous water exit of the chamber [21]. A pre-saturated soil specimen was placed on top of the disc. The sensor was placed upside down to allow the ceramic plate of the sensor to directly contact the soil specimen. In each pressure cycle, air pressure was applied to the chamber and then retained for 1 min; in turn, water in the soil was forced to flow out of the chamber through the porous ceramic disc; at equilibrium, the water potential of the soil specimen equaled the applied air pressure and quantified by the sensor. Subsequently, the pressure in the chamber was released and went back to the atmospheric pressure. Before another measurement cycle started, the soil specimen was restored to the saturated state by adding water to the soil through a valve at the lid. The soil water potential measurements were repeated for multiple cycles, starting with applying a 300 kPa air pressure to the chamber, with an incremental of 100 kPa for the next cycle, until the sensor was found dysfunctional due to the cavitation formation. Fig. 5c shows that the water potential of the soil increased dramatically upon an application of a positive air pressure to the chamber. When water was added to recover the soil to the saturated state, the sensor could report an immediate drop of the

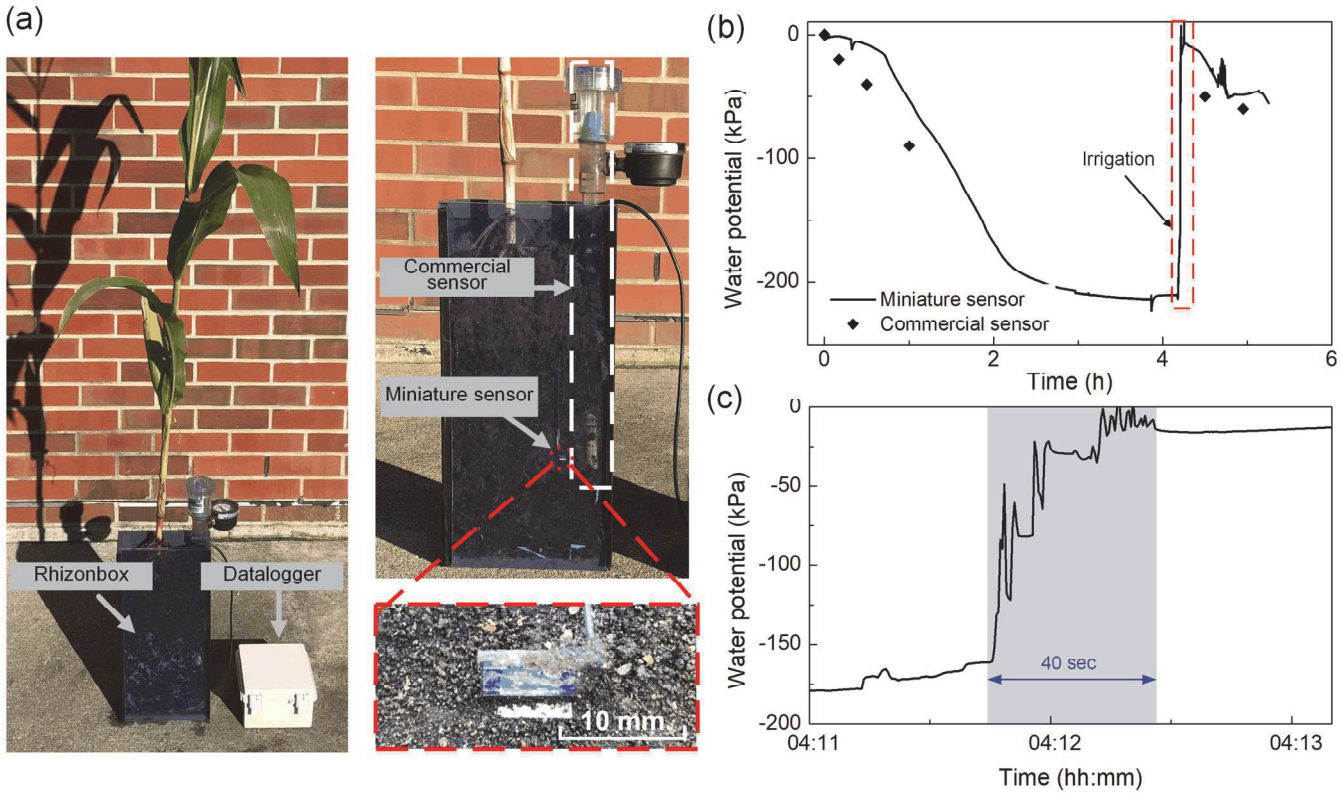

Fig. 6. (a) Continuous measurement of soil water potential inside a rhizonbox using the fabricated sensor. A bulky, long commercial sensor was used as a control device for comparion. (b) Soil water potential measured using both the fabricated sensor and the commercial sensor. (c) Close-up of the transient response of the sensor to the irrigation

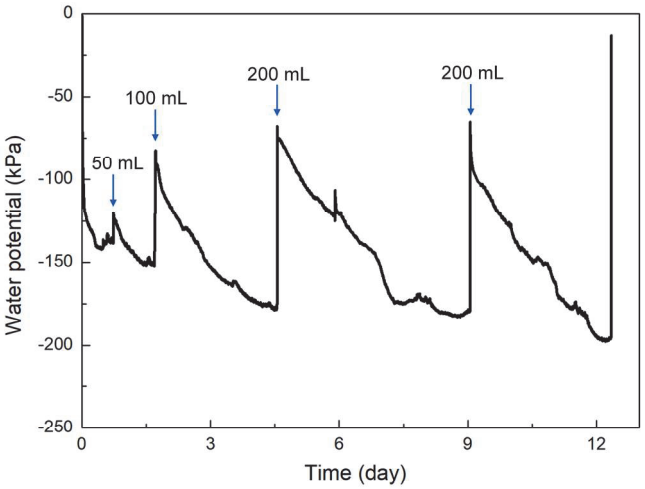

Fig. 7. Continuous measurement of soil water potential over 12 days using the sensor installed in a soil pot. The soil was irrigated for four times with different amount of water during the measurement period.

water potential. Also, the measured water potential was found close to the applied air pressure, indicating that the sensor could capture rapid changes of water potential in the soil.

IV. Laboratory and Field Demonstration

In the greenhouse, the sensor was embedded 25 cm below the soil in an acrylic rhizonbox (Fig. 6a). To facilitate the contact of the soil with the sensor, the sensor was initially wrapped with a thin layer of muddy soil. A homemade data logger was used to collect the data of water potential from the sensor during the measurement over multiple days. The data was automatically recorded and saved into a memory card of the data logger once every ten sec. A commercial tensiometer (Model SR; Irrometer) was also placed next to the sensor, serving as a control device for comparing the result from our sensor. Fig. 6b shows that 2 h after the sensor was installed, the sensor reading showed a plateau of around -200 kPa for the soil water potential, indicating the establishment of a pressure equilibrium between inside and outside the water reservoir of the sensor. When a plant was irrigated, the sensor immediately captured a dramatic drop of water potential (Fig. 6b), indicating a rapid response of the sensor to change in soil wetness. From watering on the surface of the soil to obtaining a signal from the sensor, it only took ~40 sec (Fig. 6c). The signal fluctuation observed during the ramp period may be caused by possible mechanical vibrations of the Si/SiO_2 diaphragm during reaching an equilibrium of water potential between the reservoir and the soil. The output of the sensor was found comparable to that from the commercial tensiometer. However, because the commercial tensiometer could only conduct discrete measurements with a limited dynamic range down to -100 kPa, only a few referencing data of water potential were given in Fig.

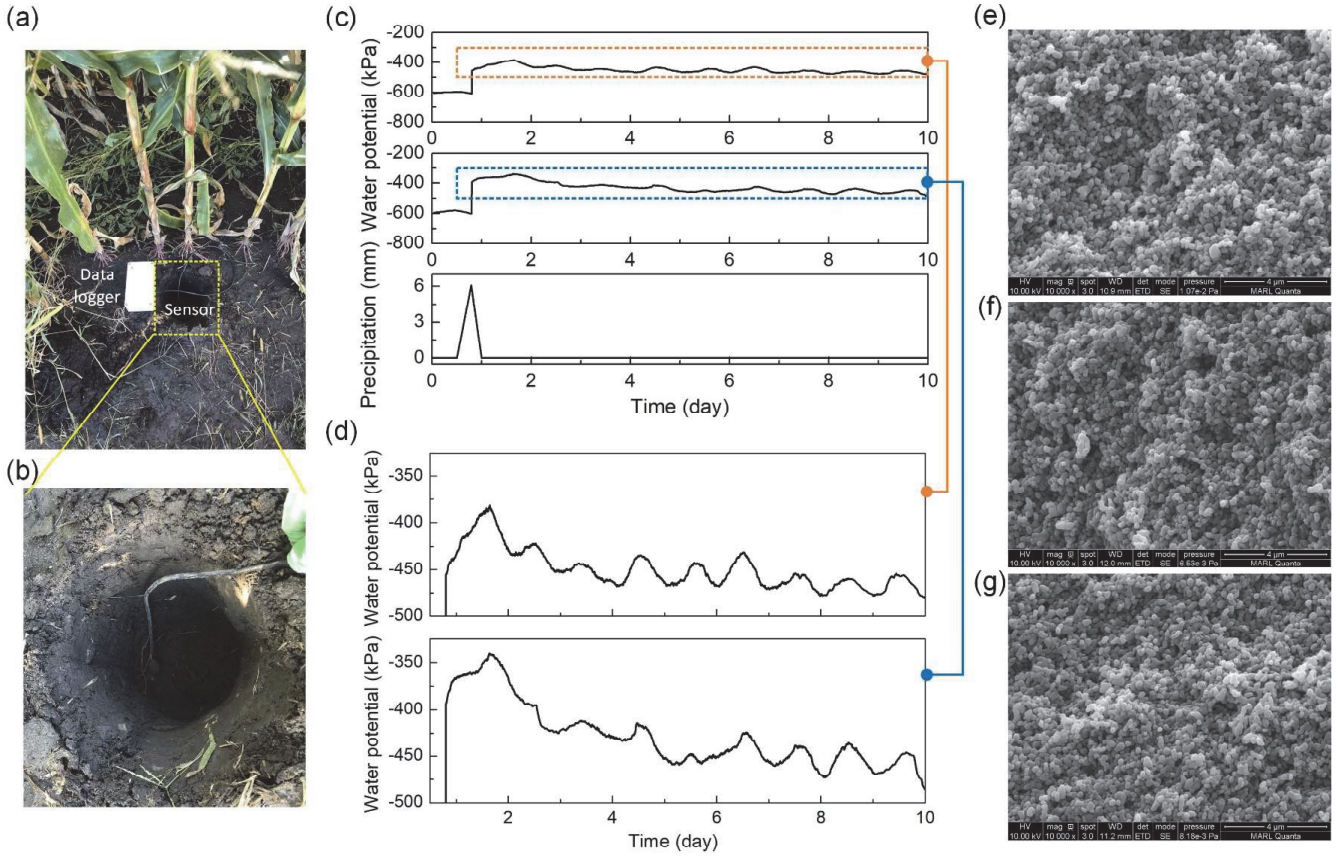

Fig. 8. (a) Installation of the soil water potential sensor in a corn field. (b) Soil water potential measured using two identical soil water potential sensors in the field. The rain precipitation was obtained by a weather station near the field. (c) Closed-up of the measured soil water potential dynamics, both showing the diurnal changes across day and night. (e)-(g) SEM photos showing the cross sectional views of the nanoporous ceramic plates in three sensors: an un-used one (e), one used for 5 days (f), and another used for 10 days (g) in the crop field.

6b. In contrast, our sensor was demonstrated to conduct continuous measurements for soil water potential.

Fig. 7 demonstrates the continuous measurement of soil water potential in a plastic soil pot in the greenhouse for twelve days. The experiment involved watering at different times and recording the response of the sensor to the irrigations. To verify whether or not the sensor could differentiate the amounts of applied water, the amounts of the first three irrigations were set to be 50 mL, 100 mL, and 200 mL, respectively. Also, to validate the consistency of the sensor measurement, the last two irrigations were applied with the same amount of water (200 mL each). The first irrigation occurred around 20 h after the sensor was installed, by pouring 50 mL tap water over the surface of the soil. Due to the irrigation, the soil water potential was found to increase by ~20 kPa immediately. Following that, as the applied water evaporated from the surface, drained out from the leakage holes at the bottom of the pot, and was absorbed by the plant, the soil became dried up gradually, thus decreasing the water potential. The second irrigation event was initiated by applying 100 mL tap water to the soil about one day after the first irrigation when the water potential drops to -155 kPa. Consequently, the water potential rapidly increased by about 80 kPa due to the irrigation, and then gradually decrease over the next three days. In the third and fourth irrigations, we poured 200 mL water to the soil, and found that the water potential for each of the two irrigations dropped by nearly the same amount of ~110 kPa, indicating that the sensor provided consistency in measurement results.

Further, a pilot field experiment with the fabricated sensors was performed in a corn field, to continuously monitor dynamic changes of soil water potential for ten days. The sensors were installed ~25 cm deep from the surface of the soil (Fig. 8a and 8b). Similarly, each sensor was coated by a thin layer of muddy soil before the installation. The daily precipitation of rain during the monitoring period was obtained from a weather station near the field on the farm. Fig. 8c demonstrates that the sensor could rapidly respond to an increase in soil wetness due to a rain event. The output of the sensor also shows that the rain led to increasing water potential from -610 kPa to -440 kPa; a few days after the rain, there was an overall trend of gradually decreasing the water potential because the soil slowly became dried. Further, it was demonstrated in Fig. 8d that the sensors were able to clearly capture diurnal changes in soil water potential across day and night; there appeared a decrease of the water potential in the day and an increase during the night. Also, when the sensors were installed close to each other, they could provide similar outputs for the local soil water potential, indicating a considerable low sensor-to-sensor variation.

Fig. 8d-8f shows the scanning electron microscopy (SEM) images for the cross-sectional views of the nanoporous ceramic plates used in three sensors, including an unused one, one that had been operating in the soil for 5 days, and another one which had been operating for 10 days. Almost no soil particles were found to enter the nanopores of the ceramic plates by capillary force or external pressure during the operation of the sensor in the soil. Our speculation is that because the size of soil particles (a few μm to a few tens of μm) is generally 2-3 orders of magnitude greater than the mean pore size of the nanopores (~80 nm), it may be not easy for soil particles to get into the nanopores even though the soil particles were in direct contact with the soil.

V. Conclusions

A miniature soil water potential sensor capable of long-term continuous measurement is reported. The sensor provides a wide dynamic range of water potential down to -800 kPa, a minimum detectable change of 40 Pa, and a high sensitivity of 0.248 μA/kPa. The sensor also offers almost instantaneous readout. To minimize the air cavitation, the sensor uses a ~80 nm-mean pore size ceramic plate to increase the air entry pressure, a shallow 200 μm-deep water reservoir with the hydrophilic interior surfaces to minimize the trapping of air bubbles. The coupling of a 200 μm-thick Si/SO_2 diaphragm with a commercial miniature optical displacement detector allows for the accurate quantification of the mechanical deflection of the diaphragm caused by changing soil water potential. The sensor has been validated in both the greenhouse and crop fields, demonstrating the ability to continuously monitor dynamic changes in water potential for ten days, conservatively. The sensor will be useful to manage irrigation in precision and digital agriculture and will contribute to obtaining high quality, high temporal resolution data on the dynamics of soil water in scientific research.

Still, there is much room to improve the presented soil water potential sensor. For example, by using a porous ceramic plate with a smaller mean pore size and higher AEV, the dynamic range of the sensor will be further improved. In addition to the direct manufacturing of the light source and photodetector [35][36] on the silicon-based diaphragm, it may also possible to develop on-chip detection mechanisms for displacement of the diaphragm (e.g., capacitive, piezoelectric, and piezoresistive methods [26][37-40]) to optimize the deflection readout from the diaphragm of the sensor. These efforts will help to further improve both the sensitivity and level of miniaturization for the sensor. Further, it is possible to realize a more powerful miniature soil sensing system for simultaneous monitoring of many other parameters (e.g., macronutrients, temperature, and moisture) that are critical to advance sustainable precision agriculture. For instance, electrochemical nutrient sensors [41-42], thermistors, moisture sensors, and energy harvesting devices [43] can be integrated on the same PCB of the presented water potential sensor to form an integrated multifunctional soil testing tool.

Acknowledgments

This work was supported in part by the United States Department of Agriculture - National Institute of Food and Agriculture under the grant number 2018-67021-27845, the United States National Science Foundation under the grant numbers IOS-1650182 and IOS-1844563, and the Plant Sciences Institute at Iowa State University. The authors also thank Dr. Michael Castellano, Dr. Patrick Schnable, and Dr. James Schnable for insightful discussions.

REFERENCES

[1] S. O. Ihuoma and C. A. Madramootoo, "Recent advances in crop water stress detection," *Computers and Electronics in Agriculture*, 141, pp. 267-275, 2017.

[2] I. B. Bame, *et al.,* "The effect of irrigation with anaerobic baffled reactor effluent on nutrient availability, soil properties and maize growth," *Agricultural Water Management*, 134, pp. 50-59, 2014

[3] Z. Xu, *et al.,* "Nutrient sensing using chip scale electrophoresis and in situ soil solution extraction," *IEEE Sensors Journal*, 17(14): pp. 4330-9, 2017.

[4] S. Irmak, "Nebraska water and energy flux measurement, modeling, and research network (NEBFLUX)," *Transactions of the ASABE*, 53(4), 1097-1115, 2010.

[5] S. Oren, *et al.,* "Tracking of water movement dynamics inside plants using leaf surface humidity sensors," In *IEEE 12th International Conference on Nano/Micro Engineered and Molecular Systems (NEMS)*, Los Angeles, CA, USA, 2017, pp. 402-405.

[6] S. Irmak, "Interannual variation in long-term center pivot–irrigated maize evapotranspiration and various water productivity response indices. I: Grain yield, actual and basal evapotranspiration, irrigation-yield production functions, evapotranspiration-yield production functions, and yield response factors," *Journal of Irrigation and Drainage Engineering*, 141(5), pp. 04014068, 2015.

[7] H. G. Jones, "Monitoring plant and soil water status: established and novel methods revisited and their relevance to studies of drought tolerance," *Journal of experimental botany*, 58(2), pp. 119-130, 2007.

[8] R. Cardoso *et al*., "A comparative study of soil suction measurement using two different high-range psychrometers," *Experimental unsaturated soil mechanics,* Springer, Berlin, Heidelberg, pp. 79-93, 2007.

[9] X. Hou *et al.*, "Calibrating Spanner psychrometers for the effects of ambient temperature: theoretical and experimental considerations," *Biosystems engineering*, 183, pp. 85-94, 2019.

[10] F. Aziz *et al*., "Influence of humidity conditions on the capacitive and resistive response of an Al/VOPc/Pt co-planar humidity sensor," *Measurement Science and Technology*, 23.1, 2011.

[11] D. Or *et al*., "Soil water content and water potential relationships," *SOIL SCIENCES*, 1999.

[12] L. A. Richards *et al*., "Soil moisture tensiometer materials and construction," *Soil Sci*, 53.4, pp.241-248, 1942.

[13] H. P. Cresswell *et al*., "The adequacy of pressure plate apparatus for determining soil water retention," *Soil Science Society of America Journal*, 72(1), pp. 41-49, 2008.

[14] P. Habasimbi *et al.*, "Soil water characteristic curve of an unsaturated soil under low matric suction ranges and different stress conditions," *International Journal of Geosciences*, 10.1, pp. 39-56, 2019.

[15] M. H. Young and J. B. Sisson, "3.2. 2 Tensiometry," in *Methods of Soil Analysis: Part 4 Physical Methods*, Madison, WI, USA, SSSA, 2002, pp. 575-608.

[16] W. R. Whalley *et al*., "Measurement of the matric potential of soil water in the rhizosphere," *Journal of experimental botany*, 64.13, 2013.

[17] D. I. Stannard *et al*., "Tensiometers—theory, construction, and use," *Geotechnical Testing Journal*, 15.1, 1992.

[18] A. M. Ridley *et al*., "Soil matrix suction: some examples of its measurement and application in geotechnical engineering," *Géotechnique*, 53.2, 2003.

[19] J. Mendes *et al*., "First Saturation and Resaturation of High Capacity Tensiometers with 1.5 MPa High Air Entry Value (HAEV) Ceramic Filters," *PanAm Unsaturated Soils*, 2017.

[20] M. Bagheri *et al*., "Cavitation in high-capacity tensiometers: effect of water reservoir surface roughness," *Geotechnical Research*, 5(2), pp. 81-95, 2018.

[21] Y. Guan *et al*., "Use of the tensile strength of water for the direct measurement of high soil suction," *Canadian Geotechnical Journal*, 34.4, 1997.

[22] ZS. Li *et al*., "Recent Developments and Applications of the High-Capacity Tensiometer in Geotechnical Engineering—A Review," *Electronic Journal of Geotechnical Engineering*, 22.6, 2016.

[23] Van Der Ploeg *et al*., "Polymer tensiometers with ceramic cones: Direct observations of matric pressures in drying soils," *Hydrology and Earth System Sciences*, 14.10, 2010.

[24] W. A., Take, and M. D. Bolton, "Tensiometer saturation and the reliable measurement of soil suction," *Géotechnique*, 53.2, 2003.

[25] V. Pagay *et al*., "A microtensiometer capable of measuring water potentials below− 10 MPa," *Lab on a Chip*, 14(15), pp. 2806-2817, 2014.

[26] J. Mendes *et al.*, "On the development of an ultra-high-capacity tensiometer capable of measuring water tensions to 7 MPa," *Géotechnique*, 69.6, pp. 560-564, 2019.

[27] A. Tarantino *et al*., "Field measurement of suction, water content, and water permeability," *Geotechnical and Geological Engineering*, 26(6), pp. 751-782, 2008.

[28] Y. Chen, *et al.,* "Miniaturized soil sensor for continuous, in-situ monitoring of soil water potential," In *IEEE 20th International Conference on Solid-State Sensors, Actuators and Microsystems & Eurosensors XXXIII (TRANSDUCERS & EUROSENSORS XXXIII)*, Berlin, Germany, 2019, pp. 2025-2028.

[29] G. Bakker *et al.*, "New polymer tensiometers: Measuring matric pressures down to the wilting point," *Vadose zone journal, 6.1*:196-202, 2007.

[30] Y. Shan *et al.,* "Low-cost IR reflective sensors for submicrolevel position measurement and control," *IEEE/ASME transactions on mechatronics*, 13(6), pp. 700-709, 2008.

[31] W. Durner and D. Or, "Soil water potential measurement," in *Encyclopedia of hydrological sciences*, Hoboken, NJ, USA: John Wiley & Sons, Inc., 2006, Ch. 73.

[32] T. Watanabe, "Wettability of ceramic surfaces-A wide range control of surface wettability from super hydrophilicity to super hydrophobicity, from static wettability to dynamic wettability," *Journal of the ceramic society of Japan*, 117.1372, pp.1285-1292, 2009.

[33] R. R. Weil, and N. C. Brady, *The Nature and Properties of Soils*, 15th ed., Columbus, Ohio, USA: Pearson, 2016, pp. 221.

[34] D. Y. Chong *et al* (December 2003). Mechanical characterization in failure strength of silicon dice. Presented in the Ninth Intersociety Conference on Thermal and Thermomechanical Phenomena, in *Electronic Systems* (IEEE Cat. No. 04CH37543). Vol. 2, IEEE.

[35] L. Dong, *et al.,* "Design and fabrication of single-chip a-Si TFT-based uncooled infrared sensors," *Sensors and Actuators A: Physical*, 116(2), pp.257-263, 2004.

[36] Y. Wang, *et al.,* "Optical bound states in slotted high-contrast gratings," *Journal of the Optical Society of America B*, 33(12), pp.2472-2479, 2016.

[37] Y.Q. Bie, *et al.,* "A MoTe 2-based light-emitting diode and photodetector for silicon photonic integrated circuits," *Nature Nanotechnology*, 12(12), pp. 1124, 2017.

[38] J. I. Lee, X. Huang, and P.B. Chu, "Nanoprecision MEMS capacitive sensor for linear and rotational positioning," *Journal of Microelectromechanical Systems*, 18(3), pp. 660-670, 2009.

[39] Q. Wang, W. Hong, and L. Dong, "Graphene "microdrums" on a freestanding perforated thin membrane for high sensitivity MEMS pressure sensors," *Nanoscale*, 8(14), pp.7663-7671, 2016.

[40] G. L. Smith, et al., "PZT-based piezoelectric MEMS technology," *Journal of the American Ceramic Society*, 95(6), pp.1777-1792, 2012.

[41] M. A. Ali, et al., "Tunable bioelectrodes with wrinkled-ridged graphene oxide surfaces for electrochemical nitrate sensors," *RSC Advances*, 6(71), pp.67184-67195, 2016.

[42] M.A. Ali, et al., "Continuous Monitoring of Soil Nitrate Using a Miniature Sensor with Poly (3-octyl-thiophene) and Molybdenum Disulfide Nanocomposite," *ACS Appl. Mater. Interfaces*, 11(32), pp.29195-29206, 2019.

[43] H. Jiang, L. J. Halverson, and L. Dong, "A miniature microbial fuel cell with conducting nanofibers-based 3D porous biofilm," *J. Micromech. Microeng.*, 25(12), pp.125017, 2015.